ROYAL SOCIETY OF CHEMISTRY

PAPER

Check for updates

A strategy to build high-performance thick electrodes for lithium-ion batteries with enhanced compressive modulus and regulated tortuosity in the phase-inversion process†

Yifan Zhang, [a] Yaohong Xiao,[b] Lei Chen[b] and Shan Hu *[a]

Building low-tortuosity thick electrodes, which is a practical strategy to boost the energy density of lithium-ion batteries (LIBs) by improving ion transport, has been investigated widely. As one of the effective and low-cost methods to form vertically aligned porous architectures, phase-inversion has been explored to enhance the performance of electrodes. Despite the achievement of electrodes with high mass loading and brilliant electrochemical performance *via* the phase-inversion process, the poor mechanical properties of electrodes impede their application in large-scale devices, such as electric vehicles (EVs). Herein, we developed a method to upgrade the compressive strength of $LiFePO_4$ (LFP) electrodes by tuning the composition of in the non-solvent used in the non-solvent induced phase-inversion based electrode fabrication. With the introduction of ethanol in the non-solvent bath, the compressive modulus of the low-tortuosity LFP electrode with a loading of 40 mg cm^{-2} reaches up to 18.1 MPa, around four times higher than that of the electrodes processed in only water with the same mass loading. Additionally, the low-tortuosity LFP electrode produced with a mixture of water and ethanol exhibits superior rate capability (73.3 mA h g^{-1} at 2C) and cycling stability (89.3% capacity retention after 100 cycles at 0.5C). Furthermore, electrodes with different mass loadings (20 and 30 mg cm^{-2}) but similar tortuosity were obtained by adjusting the duration of immersion during the phase-inversion process with the same non-solvent bath. This report provides a novel approach to enhance the mechanical robustness of high-performance thick electrodes produced through phase-inversion as well as more precise control of the microstructures.

1 Introduction

Lithium-ion batteries (LIBs) have been widely adopted in various fields ranging from consumer electronics to electric vehicles (EVs). To meet the growing demand of energy storage, high-performance LIBs have been continuously developed through new electrode materials and battery chemistries.[1–4] One of the practical strategies to improve the energy density of LIBs is to increase the thickness of their electrodes, which reduces the ratio of electrochemically inactive materials (*e.g.*, current collectors, separators, additives, and packaging materials).[5–7] In conventional design of electrodes, randomly packed particles of active materials induce high tortuosity for the pathway of lithium-ion diffusion. The relation between porosity, tortuosity, and effective diffusivity is expressed as: $D_{eff} = \varepsilon D_0/\tau$, in which

D_{eff} and D_0 represent effective and intrinsic diffusivity, respectively, and ε and τ stand for porosity and tortuosity, respectively. This indicates that a higher tortuosity decreases effective diffusivity for a given porosity in the electrode, which can result in drastic reduction in available capacity of active materials and therefore reduced energy density as the charging/discharging rate increases.[8–10] This deterioration of performance is especially severe in thick electrodes with high tortuosity.[11–13]

In recent years, various methods have been developed to engineer the architecture of electrodes to facilitate the diffusion of lithium-ions in battery electrodes, such as magnetic templating,[14,15] phase-inversion,[16–25] channel-drilling,[26,27] freeze-casting,[28–36] acoustic-field modulation,[37] nanoarray engineering,[38] stamping process,[39] and screen printing.[40] Among these novel manufacturing methods, phase-inversion is an outstanding approach in terms of efficiency and scalability for generating low-tortuosity structures.[41] For the commonly adopted procedures of battery electrode fabrication, active materials and conductive additives are dispersed in polymer binder solution to form the electrode slurry. The phase-inversion method involves three components including the

[a] Department of Mechanical Engineering, Iowa State University, 2529 Union Drive, Ames, IA 50010, USA. E-mail: shanhu@iastate.edu

[b] Department of Mechanical Engineering, University of Michigan-Dearborn, 4901 Evergreen Road, Dearborn, MI 48128, USA

† Electronic supplementary information (ESI) available. See DOI: https://doi.org/10.1039/d4ta00589a

polymer, solvent, and non-solvent, which is non-compatible or weakly compatible with the polymer. After the slurry of the battery electrode is coated on the substrate, the coating layer (with polymer binder solution) and the substrate together will be immersed in the non-solvent bath. The concentration gradient continuously drives the solvent out and the non-solvent into the polymer solution, resulting in phase separation that produces a polymer network with various microstructures inside the non-solvent.[42,43] Furthermore, due to the excellent binding between the polymer binder and the particles of active materials and conductive additives, the phase inversion of the polymer will also modulate the spatial distribution of these particles and therefore the structures of the resulting electrode. When phase inversion conditions are controlled, low-tortuosity structures such as vertically aligned channels can be formed in the battery electrodes.

Despite the advantage that the phase-inversion method has demonstrated in terms of improving the electrochemical performance of battery electrodes, the electrodes' low resistance to deformation (or low modulus), similar to electrodes with high porosity, has been one of the overdue issues that needs to be addressed.[44-46] Easy deformability because of low modulus poses a great challenge to maintain thick electrodes' mechanical robustness, which is critical for the safety and cycling stability of batteries. Compressive modulus is a critical mechanical property for thick electrodes because when electrodes are assembled into cells, they are always subjected to "compressive stack pressure" to ensure good contact between different components. In addition, during charging/discharging, an electrode will undergo volume change which can induce additional compressive stress on the electrode because they are constrained inside a battery pack.[47] In this work, we report a strategy to enhance the mechanical robustness of $LiFePO_4$ (LFP) electrodes fabricated by the phase-inversion method through tuning the composition of the non-solvent bath. Specifically, instead of using water as a non-solvent in existing work,[20,21,23] ethanol of different volume ratios was mixed with water to form the non-solvent. With a higher ratio of ethanol in the non-solvent, higher compressive modulus of low-tortuosity LFP electrodes was achieved. On the other hand, with the same areal mass loading of active materials, electrodes processed using a higher ethanol ratio showed better rate performance and cycling stability. For instance, LFP electrodes with an areal mass loading of ~40 mg cm^{-2} immersed in a non-solvent bath with 3 : 1 volumetric ratio of deionized water (DIW) to ethanol delivered a specific capacity of 73.3 mA h g^{-1} at a rate of 2C and a capacity retention of 89.3% after 100 cycles at 0.5C, compared to 37.2 mA h g^{-1} and retention of 58.2% for LFP electrodes processed using only DIW at the same rate. Moreover, with the same non-solvent, the immersion time can be adjusted for electrodes with varied thicknesses to achieve similar structural tortuosity. This investigation provides a facile phase-inversion-based method to not only promote the electrochemical performance but also improve the compressive modulus of electrodes.

2 Experimental

2.1 Preparation of low-tortuosity LFP electrodes

For the preparation of slurry, LFP powder (D_{50} = 1.5 μm, MSE supplies) and acetylene black (Alfa Aesar, 100% compressed) were dispersed in N-methyl-2-pyrrolidone (NMP) (Sigma Aldrich) solvent containing polyvinylidene fluoride (PVDF) (M_w ~180 000 g mol^{-1}, Sigma Aldrich) with the ratio of LFP, PVDF and acetylene black as 65 : 20 : 15. Mechanical stirring was applied overnight for uniform dispersion of solid materials in the slurry. The prepared slurry was cast on a glass slide to form a wet film. The thickness of the wet film is controlled using a doctor blade coater to achieve the target areal mass loading. Subsequently, the wet film is immersed in the bath of mixture of DIW and ethanol with various volume ratios (DIW : ethanol = 3 : 1, 4 : 1 and 5 : 1 or pure DIW) and time (e.g., 90 minutes for the 1.5 mm wet film in a non-solvent bath of DIW : ethanol = 3 : 1 to obtain 40 mg cm^{-2} mass loading). The electrodes were then dried at 80 °C overnight before testing.

2.2 Structural and mechanical characterization

The morphology of the surface and cross-sectional area of the as-prepared LFP electrodes was characterized by scanning electron microscopy (SEM) and energy dispersive spectroscopy (EDS) (FEI Inspect F50). The pore size distribution was measured with a mercury intrusion porosimeter (AutoPore IV 9500, Micromeritics Instrument Corporation). The compression test was performed on a RSA-G2 solids analyzer (TA Instruments). The compression test samples were placed on the platform with both fixtures of the equipment contacting the upper and bottom surfaces, respectively, at the initial status. The strain rate was set up as 0.005 mm s^{-1} and the force increased to the maximum value (35 N) before cutting off.

2.3 Electrochemical measurements

The prepared free-standing LFP electrodes were cut into disks with a diameter of 12.7 mm before coin-cell assembly. CR2032 coin-cells were built by pairing the LFP electrode and lithium chip as working and counter electrodes, respectively, with one layer of the Celgard 2400 polymer separator between two electrodes and soaked in electrolyte of 1 M LiPF$_6$ in ethylene carbonate (EC) and ethyl methyl carbonate (EMC) with the mass ratio of 3 : 7. The cells were assembled inside an argon-filled glovebox with oxygen and moisture levels less than 5 ppm. Cyclic voltammetry was performed at multiple scan rates (0.1, 0.15, 0.2 and 0.25 mV s^{-1}) within the voltage window of 2.5 to 4.2 V vs. Li$^+$/Li (Gamry Reference 3000). Electrochemical impedance spectroscopy (EIS) was performed at the frequency from 1 MHz to 0.1 Hz with an AC voltage of 10 mV on an electrochemical working station (Gamry Reference 3000). For the galvanostatic test, the cells were charged and discharged at a rate of C/20 (1C = 170 mA g^{-1}) for 2 formation cycles, followed by cycling at various C-rates between 2.5 V and 4.0 V (LANDT CT3001A).

16538 | J. Mater. Chem. A, 2024, 12, 16537–16545

This journal is © The Royal Society of Chemistry 2024

3 Results and discussion

The fabrication process of low-tortuosity LFP electrodes through the phase-inversion method is illustrated in Fig. 1. After preparing the slurry containing LFP, PVDF and acetylene black, the slurry is coated on a glass slide, and the coated electrode is immersed in a non-solvent coagulation bath which is a mixture of DIW and ethanol at varied ratios. After the phase-inversion process, the slurry coating will separate from the glass substrate and form a free-standing film, which is then taken out of the non-solvent bath and completely dried in a vacuum at 80 °C to produce the free-standing electrode. As the wet film is immersed in the non-solvent, the thermodynamic equilibrium breaks and demixing occurs in the slurry film to generate polymer-rich and polymer-lean regions. The polymer-rich region solidifies to form the skeleton or matrix of the electrode, and polymer-lean regions become macro-to nano-voids in the electrode after solvents are removed by drying in a vacuum. The introduction of ethanol (high miscibility with NMP) in DIW (low miscibility with NMP) increases the miscibility of the solvent and non-solvent, hence facilitating instantaneous demixing and the formation of finger-like channels (Fig. 1). On the other hand, with DIW as the non-solvent, more delayed demixing occurs which favors the formation of closed cellular pores in more regions of the electrode compared with the case with the mixture of DIW and ethanol (Fig. 1).[48,49] More discussion on the change of thermodynamics in phase inversion with the introduction of ethanol into the non-solvent can be found in the ESI.†

To study the influence of the ethanol ratio in the non-solvent, experiments were performed with four ratios of DIW and ethanol (3 : 1, 4 : 1, 5 : 1 and pure DIW) and the same immersion time of 90 minutes for the phase-inversion step. The areal mass loading of each electrode was controlled as ~40 mg cm^{-2} (samples are denoted as WE31-40, WE41-40, WE51-40, and DIW-40). From the scanning electron microscope (SEM) images of the four free-standing electrodes shown in Fig. 2a–d, the thickness of all four electrodes is around 850 μm. Regarding

the structure, finger-like macropores along the thickness direction and a dense skin-layer on the top surface can be clearly seen for all four samples, indicating the occurrence of phase inversion. In addition, the element mappings by energy dispersive X-ray spectroscopy (EDS) of the four electrodes are illustrated in Fig. S1 to S4,† in which uniform element distribution is observed for all four electrodes in the polymer-rich region. On the other hand, when the DIW to ethanol volume ratio is further reduced to below 3 : 1, finger-like structures can no longer be observed in the electrodes. For example, when LFP electrodes with a mass loading of ~40 mg cm^{-2} were processed with a non-solvent bath with DIW : ethanol ratios of 2 : 1, 1 : 1 and 1 : 2 for 90 minutes, there is no obvious finger-like structure observed according to the SEM images shown in Fig. S5.† Based on the existing theory and simulation work on non-solvent induced phase separation,[50–54] this phenomenon could be ascribed to the overly strong interaction between the solvent and non-solvent. The EDS of the cross-sectional area of the WE21-40 electrode (Fig. S6†) shows a polymer-rich layer with much more fluorine from the PVDF binder on the top surface than in the bulk of the electrode. Since inhomogeneous distribution of the binder is detrimental to electrochemical performance and highly undesirable for battery electrodes,[55] the investigation of this work about mechanical strength and electrochemical behaviors will focus on the LFP electrodes fabricated with a non-solvent bath with the ratio of DIW to ethanol no less than 3 : 1 during the phase-inversion process. The rate performance and tortuosity of the WE21-40 electrode, which are inferior to those of WE31-40 and WE41-40 electrodes, are nonetheless measured and included in the ESI (Fig. S22)† for reference.

To investigate the effect of varying DIW-to-ethanol ratios on mechanical properties, compressive stress and strain were measured. The stress *vs.* strain curve of each sample is plotted in Fig. 2e. To estimate the compressive modulus of each electrode, the linear region is selected to estimate the slope which equals the modulus of the electrode. As shown in Fig. 2f, compressive modulus increases when a higher concentration of
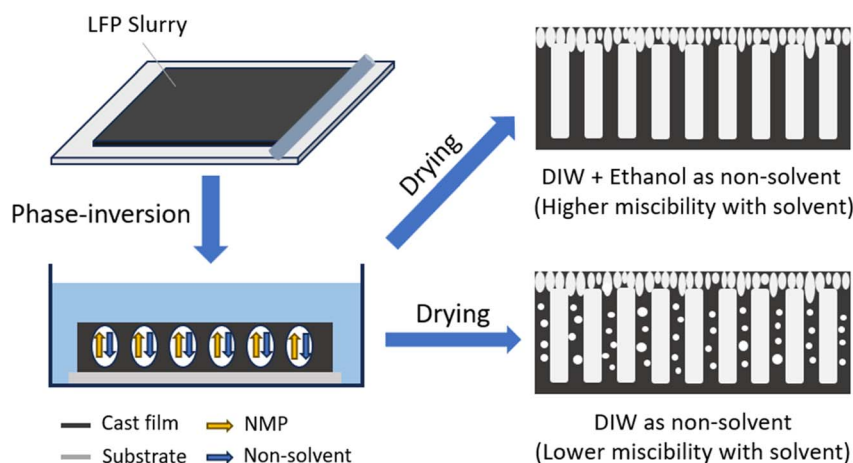

Fig. 1 The schematic of the fabrication process for the free-standing LFP electrode *via* phase-inversion processes induced by different non-solvents: mixture of DIW and ethanol and pure DIW, and their corresponding electrode structures.
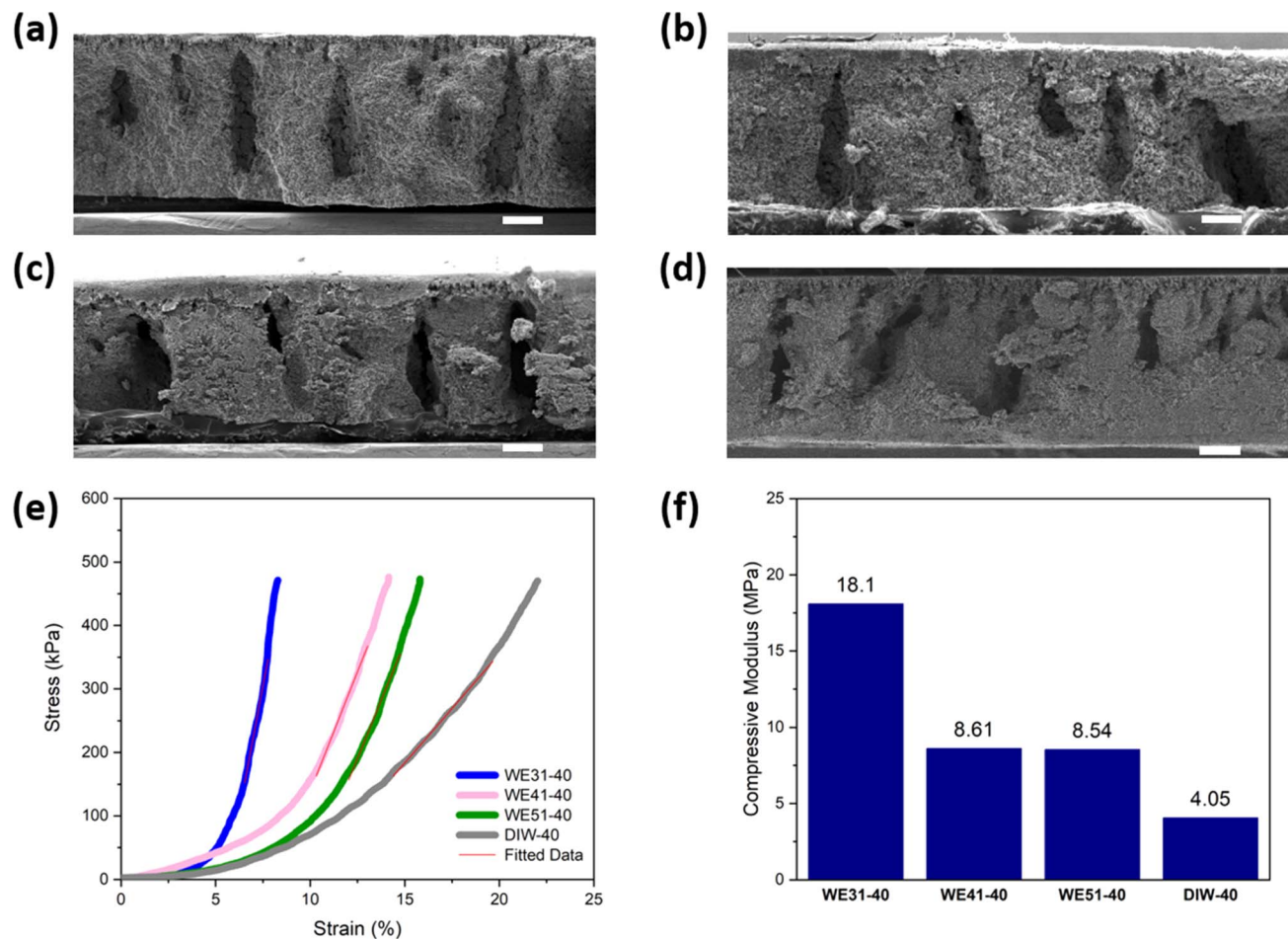
This journal is © The Royal Society of Chemistry 2024

J. Mater. Chem. A, 2024, **12**, 16537–16545 | **16539**

Fig. 2 SEM images of the cross-sectional area of (a) WE31-40, (b) WE41-40, (c) WE51-40 and (d) DIW-40 electrodes (scale bar: 200 µm); (e) stress−strain curves of the four electrodes from the compression test; (f) compression modulus of each electrode estimated from the linear part of the stress−strain curve.

ethanol was added in the non-solvent mixture. For example, the WE31-40 electrode exhibits a compressive modulus of 18.1 MPa, the highest among all four samples, compared to 4.1 MPa of the one that was only processed with DIW. Furthermore, as the applied force reaches the maximum of the testing equipment (35 N), the WE31-40 electrode shows the smallest strain compared to the other three types of electrodes. Both results indicate that the addition of ethanol during the phase-inversion process contributes to the improvement of mechanical properties of free-standing LFP electrodes. To understand the difference in compressive modulus observed in the four samples, we further investigated the microstructure of the electrode matrix, since the modulus of the electrode is mainly determined by the matrix and the four samples appear to have similar finger-like macropores. As illustrated in the high-magnification SEM image of the matrix regions (Fig. S7†), the matrix of the DIW-40 electrode has obvious closed-cell pores, whereas the WE31-40 electrode shows a more uniform structure with no obvious large pores. The pore size distribution in WE31-40 and DIW-40 electrodes is also characterized by mercury porosimetry analysis (Fig. S8†), in which WE31-40 shows more pores of sub-µm size but DIW-40 shows significantly more pores

of size around 100 µm. The mercury porosity analysis confirms the observation from the SEM images of the polymer-rich region shown in Fig. S7.† It is noted that some large finger-like pores and cellular pores that are not directly accessible through the surface but rather through a small neck will contribute to pore volume at the size of the small neck in the mercury porosimetry analysis results. Furthermore, the mercury porosimetry instrument used (AutoPore IV 9500, Micrometrics) can only measure pore sizes up to 360 µm, hence the pore size distribution shown in Fig. S8† cuts off at this value.

The rate capability of these four samples at various C-rates is compared in Fig. 3a. The results demonstrate that the four electrodes deliver similar specific discharge capacity at low C-rates (<0.5C). As the C-rate increases, however, the WE31-40 electrode retains the highest specific capacity of 152.0, 132.7 and 73.3 mA h g^{-1} at 0.5C, 1C and 2C, respectively, compared to the other three electrodes. Moreover, the electrodes produced with a higher ethanol ratio in the phase-inversion process also demonstrate lower overpotential from the voltage profiles (Fig. 3b, c and S9†). For the cycling stability (Fig. 3d), with similar areal mass loading, the electrodes fabricated with a mixture bath of ethanol and DIW all reveal an advantageous

16540 | J. Mater. Chem. A, 2024, 12, 16537–16545

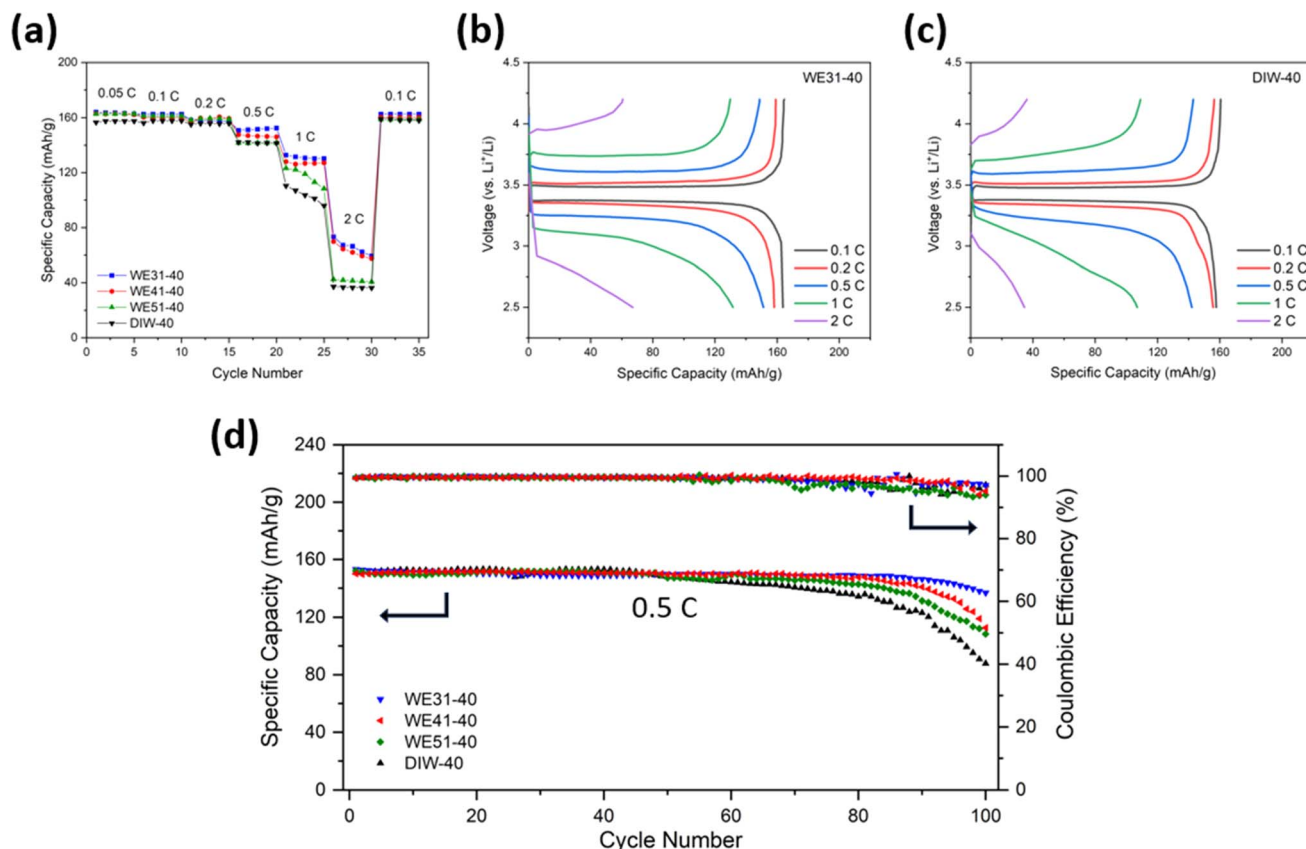This journal is © The Royal Society of Chemistry 2024

Fig. 3 (a) Rate performance of WE31-40, WE41-40, WE51-40 and DIW-40 electrodes from 0.05C to 2C; (b) voltage profile of the WE31-40 electrode during charge and discharge at various C-rates; (c) voltage profile of the DIW-40 electrode during charge and discharge at various C-rates; (d) discharge capacity and coulombic efficiency of WE31-40, WE41-40, WE51-40 and DIW-40 electrodes at 0.5C.

capacity retention of 89.3% (WE31-40), 75.1% (WE41-40) and 71.2% (WE51-40), respectively, after 100 cycles at 0.5C, compared to 57.3% for the DIW-40 electrode. After cycling, the structures inside the electrodes were well maintained according to the SEM images of the cross-sectional areas in the four electrodes shown in Fig. S10.†

To investigate the reasons behind the improved performance of electrodes prepared from the mixture of ethanol and DIW during the phase-inversion process, electrochemical impedance spectroscopy (EIS) was applied to measure the resistance of the half-cells and evaluate the kinetics of each free-standing LFP electrode. As shown in the Nyquist plot in Fig. 4a, the internal resistance (R_u) of each curve is located on the first intercept on the Re(Z) axis and charge transfer resistance (R_{ct}) can be estimated from the second intercept on the Re(Z) axis from fitting the semi-circle of each curve. The equivalent circuit to analyze EIS data is shown in the inset of Fig. 4a. A similar R_u is measured from four half cells containing the LFP electrode fabricated using different ratios of ethanol and DIW. However, with a higher ratio of ethanol in the phase-inversion process, the WE31-40 electrode demonstrates the lowest R_{ct} of 52.9 Ω among these four electrodes, while DIW-40 possessed the highest resistance of 83.6 Ω for charge transfer. In the low-frequency region, according to the semi-infinite linear diffusion and eqn (S3),† the Warburg coefficient (σ) can be obtained by linearly fitting the Warburg impedance (Z_W)

versus reverse square root of angular frequency ($\omega^{-1/2}$). Based on the relation between diffusion coefficients of lithium-ions (D_{Li^+}) and the Warburg coefficient expressed using eqn (S4),† D_{Li^+} can be calculated with the low-frequency data of the EIS. For example, the WE31-40 electrode reveals the highest D_{Li^+} of 6.70×10^{-9} cm^2 s^{-1} compared to the other three LFP electrodes (Table S2†), demonstrating that lithium-ion diffusion is facilitated in electrodes fabricated with the non-solvent bath containing a higher ratio of ethanol in the phase-inversion process. Additionally, cyclic voltammetry (CV) is implemented to study the kinetics of these four electrodes. From the cyclic voltammograms, which were recorded at a scan rate of 0.1 mV s^{-1}, illustrated in Fig. 4c, the WE31-40 electrode exhibits the highest peak current in both anodic and cathodic regions and the smallest gap between the peaks, which indicates the lowest overpotential. As the ethanol ratio decreases in the non-solvent bath, lower peak current and larger overpotential of the as-prepared electrodes are demonstrated (Fig. S11†). These results indicate that for the phase-inversion-based electrode fabrication process, lithium-ion diffusion and reaction kinetics are enhanced for the electrodes as the ethanol-to-DIW ratio increases in the non-solvent bath. It is noted that the D_{Li^+} measured from Warburg impedance analysis reflects mostly the through-plane diffusion, which will benefit from the finger-like channels along the thickness direction created by the phase inversion process.
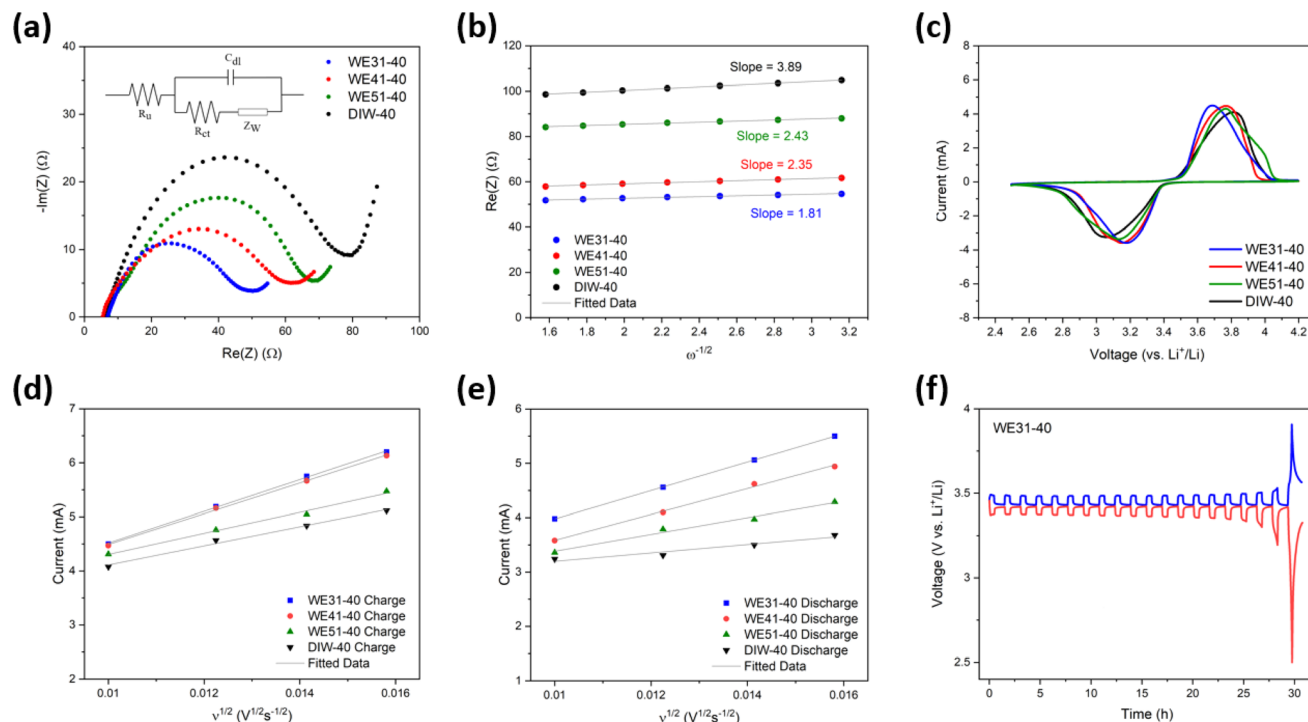
Fig. 4 (a) Nyquist plots of WE31-40, WE41-40, WE51-40 and DIW-40 electrodes; (b) real impedance of the low-frequency region from Nyquist plots and fitted data of impedance *vs.* inverse square root of angular frequency ($\omega^{-1/2}$); (c) cyclic voltammograms of WE31-40, WE41-40, WE51-40 and DIW-40 electrodes at a scan rate of 0.1 mV s; linearly fitted data of peak current *vs.* square root of scan rate in (d) anodic and (e) cathodic regions of cyclic voltammograms. (f) GITT profile of the WE31-40 electrode.

Additionally, the galvanostatic intermittent titration technique (GITT) was applied to evaluate the lithium-ion diffusion for the fabricated electrodes. As shown in Fig. 4f, a similar static potential was demonstrated by all four electrodes (∼3.43 V). With a higher ratio of water during the phase-inversion process, however, the electrode shows a larger overpotential, which indicates larger resistance in the cell (Fig. S13†). Lithium-ion diffusion coefficients of each electrode are estimated from the GITT measurement as 4.90×10^{-10}, 4.36×10^{-10}, 2.97×10^{-10}, and 1.30×10^{-10} cm^2 s^{-1} for WE31-40, WE41-40, WE51-40, and DIW-40, respectively. The trend of D_{Li^+} from GITT measurement is consistent with that from the EIS measurement, further validating the benefits in electrochemical performances brought by using higher ethanol-to-DIW ratios in the non-solvent bath. The detailed procedure of obtaining diffusion coefficients from the data *via* GITT measurement is provided in the ESI.†

Tortuosity of the electrode describes the degree of twisting for lithium-ion diffusion pathways in the electrode. It is one of the key factors that affects the kinetics of the electrode. In this work, tortuosity of the as-prepared LFP electrodes was measured *via* the DC-polarization method with a symmetric cell model shown in the inset of Fig. 5a. Note that because of the configuration of the symmetric cell, the measured tortuosity reflects mostly through-plane tortuosity. In the symmetric cell, the free-standing LFP electrode is sandwiched by two layers of the polymer separator and lithium chip on each side. As shown in Fig. 5a, a small current is initially applied to generate

a concentration gradient in the cell, followed by relaxing. The same method was applied to measure the intrinsic diffusivity of the electrolyte, where instead of the free-standing LFP electrode, the PTFE O-ring is used to separate the two layers of the polymer separator and lithium chips on each side as shown in Fig. S14.† The measured intrinsic diffusivity of the electrolyte is 9.59×10^{-7} cm^2 s^{-1}, which matches the value in the literature.[56,57] For the measurements of the four electrodes fabricated using varied ratios of ethanol to DIW, the tortuosity is 7.85, 9.76, 14.1 and 15.1 for WE31-40, WE41-40, WE51-40, and DIW-40, respectively, as illustrated in Fig. 5b and c. These results confirm that a higher ratio of ethanol assists to build electrodes with lower tortuosity, which boosts the lithium-ion diffusion, leading to the improvement in kinetics and rate performance. Moreover, the enhanced ion transport contributes to decreasing the overpotential, which improves the cycling stability of the cell.

Besides the composition of the non-solvent, we discovered that the immersion time is another key factor that affects the structure of the electrodes fabricated by the phase inversion method. For a wet film of the same composition but different thicknesses and hence different areal mass loadings, the immersion time can be adjusted to achieve similar tortuosity in the as-fabricated electrodes. LFP electrodes with areal mass loadings of 20, 30 and 40 mg cm^{-2} were prepared using the same non-solvent (DIW : ethanol volumetric ratio of 3 : 1) and denoted as WE31-20, WE31-30, and WE31-40 respectively. When controlling the immersion time to be 15, 45 and 90 min, respectively, all three electrodes achieve similar finger-like
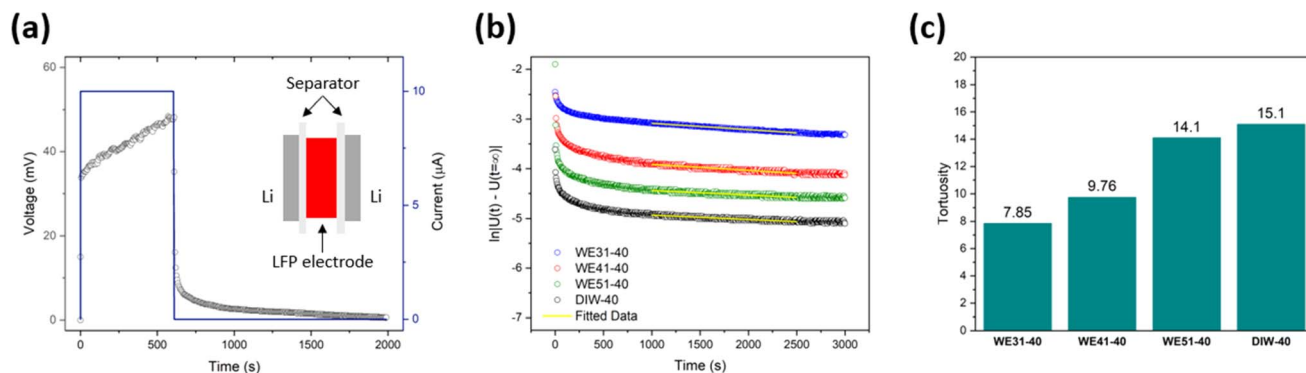
16542 | *J. Mater. Chem. A*, 2024, **12**, 16537–16545

This journal is © The Royal Society of Chemistry 2024

Fig. 5 (a) Voltage change and current applied in DC-polarization (inset: schematic picture of parts in the symmetric cell for tortuosity measurement); (b) Plots of $\ln|U(t) - U(t = \infty)|$ versus time of WE31-40, WE41-40, WE51-40 and DIW-40 electrodes and fitted data of the linear region in each plot; (c) estimated tortuosity of each electrode based on the fitted data of DC-polarization.

structures (Fig. 2a and S15†). Moreover, the tortuosity of WE31-20, WE31-30, and WE31-40, as measured by the DC-polarization method, is almost the same at 7.44, 7.64 and 7.85, respectively (Fig. 6a). To further study how the immersion time affects the tortuosity, using a nonsolvent bath with a water : ethanol 3 : 1 v/v ratio, we prepared electrodes of the same mass loading (20 mg cm^{-2}) but subjected to different immersion times (10 min, 15 min, 30 min, 45 min), denoted as WE31-20-10 min to WE31-20-45 min. The tortuosity of these samples was measured by DC-polarization tests. Based on the results shown in Fig. S16 and

Table S6,† for the areal mass loading and immersion time studied, there is an increasing trend for tortuosity as the immersion time increases. These results show the tortuosity of the electrode prepared by the phase inversion process can be modulated by varying the immersion time.

The electrochemical performances of the WE31-20 and WE31-30 samples are also characterized and compared with those of WE31-40. The Nyquist plot (Fig. 6b) shows that the charge transfer resistances of WE31-20 and WE31-30 are 31.1 and 35.9 Ω, respectively, compared to a value of 52.9 Ω for
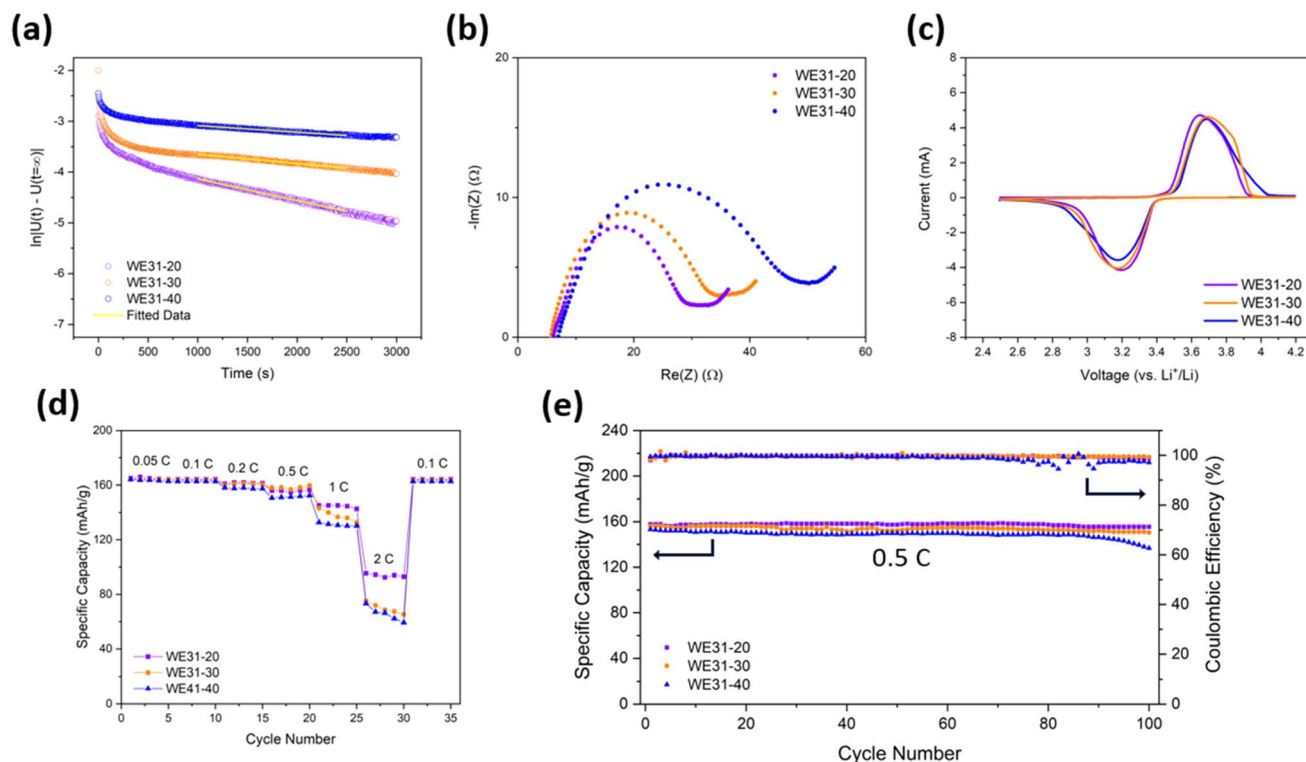

Fig. 6 (a) Plots of $\ln|U(t) - U(t = \infty)|$ versus time of WE31-20, WE31-30 and WE31-40 electrodes and fitted data of the linear region in each plot; (b) Nyquist plots of WE31-20, WE31-30 and WE31-40 electrodes; (c) cyclic voltammograms of WE31-20, WE31-30 and WE31-40 electrodes at a scan rate of 0.1 mV s; (d) rate performance of WE31-20, WE31-30 and WE31-40 electrodes from 0.05C to 2C; (e) discharge capacity and coulombic efficiency of WE31-20, WE31-30 and WE31-40 electrodes at 0.5C.

This journal is © The Royal Society of Chemistry 2024

J. Mater. Chem. A, 2024, **12**, 16537–16545 | **16543**

WE31-40. The lithium-ion diffusion coefficients of 1.55×10^{-8} $cm^2\ s^{-1}$ for WE31-20 and $1.19 \times 10^{-8}\ cm^2\ s^{-1}$ for WE31-30 were estimated from the low-frequency region of the electrochemical impedance spectra (Fig. S17†), both of which are slightly higher than the diffusion coefficient of $6.70 \times 10^{-9}\ cm^2\ s^{-1}$ for WE31-40 measured by the same method. The slightly better Li^+ diffusion in WE31-20 and WE31-30 is mainly ascribed to the lower mass loading. Their narrow advantages on mass transport over the WE31-40 electrode are also reflected in the cyclic voltammograms as the two electrodes with less mass loading demonstrate higher peak current and smaller peak distance (Fig. 6c). Furthermore, the GITT data (Fig. S21†) indicate smaller overpotential and better lithium-ion diffusion for WE31-20 ($1.50 \times 10^{-9}\ cm^2\ s^{-1}$) and WE31-30 ($1.18 \times 10^{-9}\ cm^2$ s^{-1}) electrodes compared to the WE31-40 electrode ($4.90 \times 10^{-10}\ cm^2\ s^{-1}$). For the rate performance shown in Fig. 6d, the three electrodes share a similar rate capability when the C-rate is under 1C, where discharge specific capacities of the three electrodes differ by less than 10 mA h g^{-1} at each corresponding rate. As the C-rate goes up to 2C, the WE31-20 electrode exhibits an excellent performance of 95.4 mA h g^{-1} compared to the other electrodes, which is expected since this electrode has the smallest tortuosity and thickness (areal mass loading) among the three samples. For cycling stability, the lower resistance and improved kinetics assist the electrodes with less mass loading to maintain a more stable capacity retention after 100 cycles of charge and discharge at 0.5C as shown in Fig. 6e. In summary, similar tortuosity in the electrodes with varied areal mass loadings is successfully achieved with the same non-solvent composition during phase-inversion fabrication by adjusting the immersion time. Largely similar electrochemical performances were demonstrated by the three electrodes with similar tortuosity but different areal mass loadings, with the electrode having the smallest loading inevitably showing a small margin of performance advantage.

4 Conclusion

In conclusion, we demonstrate an approach to not only construct low-tortuosity structures in electrodes with high areal mass loading to facilitate lithium-ion diffusion for high performance, but also improve the compressive modulus by tuning the composition of the non-solvent in phase-inversion fabrication. To achieve these two targets, ethanol is mixed with deionized water at various ratios to form the non-solvent bath in the phase-inversion process. As a comparison to the LFP electrode processed with only water, the electrodes processed with a mixture of water and ethanol provide a higher compressive modulus. Moreover, the LFP electrode fabricated using the non-solvent with ethanol exhibits an advantageous rate performance and cycling stability. Additionally, similar tortuosity was successfully achieved in the free-standing LFP electrodes of various thicknesses by regulating the immersion time in the same non-solvent. This work advances the phase-inversion based method for fabricating low-tortuosity battery electrodes, in that it provides an effective strategy to build low-tortuosity thick electrodes for LIBs with high performance along with enhanced mechanical properties and more precise control of the microstructure in the electrode.

Conflicts of interest

The authors have no conflict of interest.

Acknowledgements

References

1 J. B. Goodenough and K. S. Park, *J. Am. Chem. Soc.*, 2013, **135**, 1167–1176.

2 N. Nitta, F. Wu, J. T. Lee and G. Yushin, *Mater. Today*, 2015, **18**, 252–264.

3 Y. Liu, Y. Zhu and Y. Cui, *Nat. Energy*, 2019, **4**, 540–550.

4 J. Li, J. Fleetwood, W. B. Hawley and W. Kays, *Chem. Rev.*, 2021, **122**, 903–956.

5 J. Chang, Q. Huang, Y. Gao and Z. Zheng, *Adv. Mater.*, 2021, **33**, 2004419.

6 Y. Kuang, C. Chen, D. Kirsch and L. Hu, *Adv. Eng. Mater.*, 2019, **9**, 1901457.

7 Y. Chen, B. Zhao, Y. Yang and A. Cao, *Adv. Eng. Mater.*, 2022, **12**, 2201834.

8 M. Ebner, D. W. Chung, R. E. García and V. Wood, *J. Power Sources*, 2009, **188**, 592–600.

9 I. V. Thorat, D. E. Stephenson, N. A. Zacharias, K. Zaghib, J. N. Harb and D. R. Wheeler, *J. Power Sources*, 2009, **188**, 592–600.

10 H. Zheng, J. Li, X. Song, G. Liu and V. S. Battaglia, *Electrochim. Acta*, 2012, **71**, 258–265.

11 M. J. Lain and E. Kendrick, *J. Power Sources*, 2021, **493**, 229690.

12 Z. Du, D. L. Wood, C. Daniel, S. Kalnaus and J. Li, *J. Appl. Electrochem.*, 2017, **47**, 405–415.

13 X. Zhang, Z. Ju, Y. Zhu, K. J. Takeuchi, E. S. Takeuchi, A. C. Marschilok and G. Yu, *Adv. Eng. Mater.*, 2021, **11**, 2000808.

14 L. Li, R. M. Erb, J. Wang, J. Wang and Y. M. Chiang, *Adv. Eng. Mater.*, 2019, **9**, 1802472.

15 J. S. Sander, R. M. Erb, L. Li, A. Gurijala and Y. M. Chiang, *Nat. Energy*, 2016, **1**, 16099.

16 C. T. C. Wan, R. R. Jacquemond, Y. M. Chiang, K. Nijmeijer, F. R. Brushett and A. Forner-Cuenca, *Adv. Mater.*, 2021, **33**, 2006716.

17 F. Shen, R. A. Jonson, D. Y. Parkinson and M. C. Tucker, *J. Am. Ceram. Soc.*, 2022, **105**, 90–98.

16544 | *J. Mater. Chem. A*, 2024, **12**, 16537–16545

This journal is © The Royal Society of Chemistry 2024

18 M. R. Asghar, Y. Zhang, A. Wu, X. Yan, S. Shen, C. Ke and J. Zhang, *J. Power Sources*, 2018, **379**, 197–205.

19 J. Wang, M. Wang, N. Ren, J. Dong, Y. Li and C. Chen, *Energy Storage Mater.*, 2021, **39**, 287–293.

20 J. Wu, Z. Ju, X. Zhang, K. J. Takeuchi, A. C. Marschilok, E. S. Takeuchi and G. Yu, *Nano Lett.*, 2021, **21**, 9339–9346.

21 J. Wang, M. Wang, J. Si, Y. Zhu and C. Chen, *Chem. Eng. J.*, 2023, **451**, 138651.

22 J. Wu, Z. Ju, X. Zhang, X. Xu, K. J. Takeuchi, A. C. Marschilok, E. S. Takeuchi and G. Yu, *ACS Nano*, 2022, **16**, 4805–4812.

23 J. Wu, Z. Ju, X. Zhang, C. Quilty, K. J. Takeuchi, D. C. Bock, A. C. Marschilok, E. S. Takeuchi and G. Yu, *ACS Nano*, 2021, **15**, 19109–19118.

24 W. Wahyudi, Z. Cao, P. Kumar, M. Li, Y. Wu, M. N. Hedhili, T. D. Anthopoulos, L. Cavallo, L. J. Li and J. Ming, *Adv. Funct. Mater.*, 2018, **28**, 1802244.

25 A. B. Resing, C. Fukuda and J. G. Werner, *Adv. Mater.*, 2023, **35**, 2209694.

26 K. H. Chen, M. J. Namkoong, V. Goel, C. Yang, S. Kazemiabnavi, S. M. Mortuza, E. Kazyak, J. Mazumder, K. Thornton, J. Sakamoto and N. P. Dasgupta, *J. Power Sources*, 2020, **471**, 228475.

27 H. Wang, J. Li, Z. Miao, K. Huang, Y. Liao, X. Xu, J. Meng, Z. Li and Y. Huang, *ACS Appl. Mater. Interfaces*, 2023, **15**, 26824–26833.

28 D. Dang, Y. Wang, S. Gao and Y. T. Cheng, *Carbon*, 2020, **159**, 133–139.

29 B. Delattre, R. Amin, J. Sander, J. De Coninck, A. P. Tomsia and Y.-M. Chiang, *J. Electrochem. Soc.*, 2018, **165**, A388–A395.

30 Y. Hwa, E. Yi, H. Shen, Y. Sung, J. Kou, K. Chen, D. Y. Parkinson, M. M. Doeff and E. J. Cairns, *Nano Lett.*, 2019, **19**, 4731–4737.

31 G. Du, Y. Zhou, X. Tian, G. Wu, Y. Xi and S. Zhao, *Appl. Surf. Sci.*, 2018, **453**, 493–501.

32 Y. Guo, Y. Jiang, Q. Zhang, D. Wan and C. Huang, *J. Power Sources*, 2021, **506**, 230052.

33 S. Yang, C. Zhou, Q. Wang, B. Chen, Y. Zhao, B. Guo, Z. Zhang, X. Gao, R. Chowdhury, H. Wang, C. Lai, N. P. Brandon, B. Wu and X. Liu, *Energy Environ. Mater.*, 2022, **5**, 1332–1339.

34 X. Zhang, Z. Hui, S. King, L. Wang, Z. Ju, J. Wu, K. J. Takeuchi, A. C. Marschilok, A. C. West, E. S. Takeuchi and G. Yu, *Nano Lett.*, 2021, **21**, 5896–5904.

35 X. Zhang, Z. Ju, L. M. Housel, L. Wang, Y. Zhu, G. Singh, N. Sadique, K. J. Takeuchi, E. S. Takeuchi, A. C. Marschilok and G. Yu, *Nano Lett.*, 2019, **19**, 8255–8261.

36 C. Huang, M. Dontigny, K. Zaghib and P. S. Grant, *J. Mater. Chem. A*, 2019, **7**, 21421–21431.

37 Y. Zhang, M. Shahriar and S. Hu, *J. Mater. Chem. A*, 2023, **11**, 11849–11858.

38 T. Meng, Z. Geng, F. Ma, Y. Liu, X. Xu and H. Zhang, *Electrochim. Acta*, 2023, **450**, 142268.

39 H. Ren, Y. Wang, D. Cao, W. Gedney, T. Ji, X. Sun and H. Zhu, *Energy Environ. Mater.*, 2023, **6**, e12584.

40 Y. Wang, Y. Zhang, D. Cao, T. Ji, H. Ren, G. Wang, Q. Wu and H. Zhu, *Small Methods*, 2023, **7**, 2201344.

41 X. Yang, Y. Chen, M. Wang, H. Zhang, X. Li and H. Zhang, *Adv. Funct. Mater.*, 2016, **26**, 8427–8434.

42 S. Ashtiani, M. Khoshnamvand, P. Číhal, M. Dendisová, A. Randová, D. Bouša, A. Shaliutina-Kolešová, Z. Sofer and K. Friess, *RSC Adv.*, 2020, **10**, 40373–40383.

43 G. R. Guillen, Y. Pan, M. Li and E. M. V. Hoek, *Ind. Eng. Chem. Res.*, 2011, **50**, 3798–3817.

44 Z. Wang, C. Dai, K. Chen, Y. Wang, Q. Liu, Y. Liu, B. Ma, L. Mi and W. Mao, *J. Power Sources*, 2022, **551**, 232176.

45 D. J. Arnot, K. S. Mayilvahanan, Z. Hui, K. J. Takeuchi, A. C. Marschilok, D. C. Bock, L. Wang, A. C. West and E. S. Takeuchi, *Acc. Mater. Res.*, 2022, **3**, 472–483.

46 C. Chen, Y. Zhang, Y. Li, Y. Kuang, J. Song, W. Luo, Y. Wang, Y. Yao, G. Pastel, J. Xie and L. Hu, *Adv. Energy Mater.*, 2017, **7**, 1700595.

47 J. Cannarella and C. B. Arnold, *J. Power Sources*, 2014, **245**, 745–751.

48 A. Bowino, G. Capannelli, S. Munari and A. Turturro, *J. Polym. Sci., Part B: Polym. Phys.*, 1988, **26**, 785–794.

49 W. Lu, Z. Yuan, Y. Zhao, H. Zhang, H. Zhang and X. Li, *Chem. Soc. Rev.*, 2017, **46**, 2199–2236.

50 D. R. Tree, L. F. Dos Santos, C. B. Wilson, T. R. Scott, J. U. Garcia and G. H. Fredrickson, *Soft Matter*, 2019, **15**, 4614–4628.

51 C. E. Udoh, V. Garbin and J. T. Cabral, *Langmuir*, 2016, **32**, 8131–8140.

52 J. G. Wijmans, H. J. J. Rutten and C. A. Smolders, *J. Polym. Sci., Polym. Phys. Ed.*, 1985, **23**, 1941–1955.

53 A. J. Reuvers and C. A. Smolders, *J. Membr. Sci.*, 1987, **34**, 67–86.

54 C. Cohen, G. B. Tanny and S. Prager, *J. Polym. Sci., Polym. Phys. Ed.*, 1979, **17**, 477–489.

55 T. Lombardo, A. C. Ngandjong, A. Belhcen and A. A. Franco, *Energy Storage Mater.*, 2021, **43**, 337–347.

56 M. T. Ong, O. Verners, E. W. Draeger, A. C. T. Van Duin, V. Lordi and J. E. Pask, *J. Phys. Chem. B*, 2015, **119**, 1535–1545.

57 A. Nyman, M. Behm and G. Lindbergh, *Electrochim. Acta*, 2008, **53**, 6356–6365.